

Article

Anisotropic Hardening of HC420 Steel Sheet: Experiments and Analytical Modeling

Thamer Sami Alhalaybeh , Hammad Akhtar, Ashiq Iqbal Chowdhury  and Yanshan Lou 

School of Mechanical Engineering, Xi'an Jiao Tong University, 28 Xianning West Road, Xi'an 710049, China; thamersami@stu.xjtu.edu.cn (T.S.A.); ha.mes@stu.xjtu.edu.cn (H.A.); ashig@stu.xjtu.edu.cn (A.I.C.)

* Correspondence: ys.lou@xjtu.edu.cn; Tel.: +86-29-82668602

Abstract: Choosing the appropriate yield function is essential to precisely predicting the anisotropic hardening behavior of steel metals considering general loading directions. This research investigates the anisotropic hardening behavior of HC420 steel sheet by combining experimental and analytical modeling. Experiments are conducted for uniaxial tensile tests according to the three different directions and bulging tests to obtain hardening data. The experimental findings show that the loading direction affects the anisotropic behavior of HC420 steel's strength and plastic deformation. The Chen-coupled quadratic and non-quadratic (Chen-CQN) approach is used to ensure the convexity of the HC420 steel. By comparing the Chen-CQN approach with the Yld2000-2d and Stoughton-Yoon'2009 yield functions, the Chen-CQN approach shows superiority in predicting the hardening behavior of the HC420 sheet, exhibiting a more straightforward numerical implementation and enhanced accuracy in yield stress predictions under different loading directions. Results from experimental hardening tests reveal that the Chen-CQN function precisely and flexibly characterizes the yield surface of HC420 steel, with a constant variation of within 2% from its predictions.

Keywords: anisotropic hardening; plastic deformation; yield function; convexity



Academic Editor: Andrii Kostryzhev

Received: 20 December 2024

Revised: 26 January 2025

Accepted: 29 January 2025

Published: 1 February 2025

Citation: Alhalaybeh, T.S.; Akhtar, H.; Chowdhury, A.I.; Lou, Y. Anisotropic Hardening of HC420 Steel Sheet: Experiments and Analytical Modeling. *Metals* **2025**, *15*, 149. <https://doi.org/10.3390/met15020149>

Copyright: © 2025 by the authors. Licensee MDPI, Basel, Switzerland. This article is an open access article distributed under the terms and conditions of the Creative Commons Attribution (CC BY) license (<https://creativecommons.org/licenses/by/4.0/>).

1. Introduction

High-strength, cold-rolled steel sheet HC420 has been widely applied in various fields due to its excellent mechanical properties, especially in the field of structures and automobiles [1]. This steel is especially suitable for the requirement of lightweight design; its well-balanced strength and ductility ensure a much better vehicle performance with higher fuel efficiency. Reliability and maximum performance can only be guaranteed when the anisotropic behavior of this material is taken well into consideration in the forming processes [2]. Given the hardening properties of HC420, the choice of an adequate yield function becomes quite important with the increasing request for complex materials in industrial applications [3]. Detailed numerical simulations of material behavior throughout the whole forming process will hence be possible, enabling accurate mechanical performance predictions and meeting the requirements concerning the durability and safety of practical engineering applications [4]. The study on the yield behavior of metallic materials has resulted in the formulation of various yield criteria [5]. Different anisotropic yield functions [6–8] are used to improve the prediction accuracy of strong anisotropic behaviors, typically applied under the plane stress condition to effectively characterize the anisotropy of yield surfaces. The Hill48 yield criterion, which has added four non-uniform parameters to the von Mises yield function [9], is one of the most important early contributions. This

model is still in wide use because of its accuracy in predicting uniaxial and equibiaxial tensile hardening characteristics in the rolling direction (RD), diagonal direction (DD), and transverse direction (TD) loading directions. Although it is effective, the quadratic form of Hill48 limits its ability to distinguish yield surfaces for metals exhibiting different crystal structures [10]. To resolve this problem, Hosford proposed an exponential expression that includes the yield behavior of face-centered cubic (FCC) and body-centered cubic (BCC) metals [11]. Then, using linear transformation tensors, Barlat et al. [12] extended isotropic functions to anisotropy, producing models like Yld2000-2d for plane stress states and Yld2004-18p for spatial stress states. Cazacu et al. [13] made another breakthrough by using primary stress deviation data to develop an orthogonal anisotropic yield model that accounts for tension–compression asymmetry [14]. To further characterize the yield surfaces, other researchers have investigated methods relying on stress invariants. In an attempt to more accurately describe the asymmetry between tension and compression, Yoon et al. [15] developed an asymmetric model involving the first invariant. To explain the anisotropic behavior of BCC and FCC metals in complicated processes such as deep drawing, as noted in investigations of aluminum alloys, Lou et al. [16] further developed these models by accounting for the influence of third invariants. Also, the pressure-sensitive Drucker yield function was developed to take into account the combined effects of strength asymmetry, Lode angle, and pressure on yield behavior [17]. Such developments have paved the way for anisotropic hardening models to use parameterized anisotropy coefficients explaining the changes in yield surfaces [18,19]. Lee et al. [20] used the CQN model, which combines the quadratic and Hershey–Hosford functions, with which the hardening tendencies reported are in good agreement. In the meantime, Hu et al. [21] developed a fourth-order polynomial-based yield criterion to describe anisotropic evolution, while Hou et al. [22] suggested an anisotropic hardening model to bridge the Hill48 function with stress-invariant models.

Many researchers have provided insight into the yield behavior and plastic anisotropy under plane stress loading [23–27]. Barlat et al. [28] focused on linear transformations of stress tensors to describe the anisotropy of plastic properties. Barlat et al. [29] studied the plastic behavior and ductility of sheet metal under plane stress conditions. Hou et al. [30] studied the experimental characterization and modeling of complex anisotropic hardening in quenching and splitting steels subjected to biaxial disproportionate loads. While great progress has been achieved, predicting stress-state effects on flow curves and precisely capturing different strain-hardening responses remains a difficulty [31,32]. Continued attempts to combine experimental data and enhance yield functions are critical to improve our knowledge of anisotropic yield behavior [33–36]. Du et al. [37] proposed the CPN2025 yield stress function to accurately characterize plastic anisotropy under diverse loading conditions. They compared the CPN2025 model with other non-associated functions, including S-Y 2009, CQN2017, and NAFR-Poly4, demonstrating that CPN2025 exhibits superior flexibility and accuracy, particularly in near-plane strain tension and simple shear scenarios.

In this study, the hardening behavior of HC420 steel is investigated through tensile and bulging tests along three directions, i.e., RD, DD, and TD. Three anisotropic yield functions are selected to describe the anisotropic hardening behavior of HC420 steel, with their convexity ensured using the dichotomy method. The effectiveness of these yield functions in predicting the hardening curves of HC420 steel is compared, with a focus on the Chen-CQN function due to its simplicity and high precision in numerical applications. The performance of the Chen-CQN function is further validated by comparing its predicted hardening curves with experimental results, demonstrating its suitability for accurately predicting the plastic deformation of HC420 steel. This work provides a reliable

approach for characterizing the anisotropic hardening behavior of HC420 steel, supporting its application in lightweight automotive designs and numerical simulations.

2. Experiments

Dogbone specimens designed with a thickness of 1.20 mm were used to perform uniaxial tensile tests, and bulging specimens with the same thickness were used for forming limit curves tests of HC420 steel, as shown in Figure 1. The dogbone specimens were cut from sheet metal using a laser cutting machine in three directions, consecutively: RD, DD, and TD. A stochastic pattern was applied to the HC420 sheet metal, as it provides uniform and controlled conditions, ensuring the reliability and repeatability of the tensile test results critical for accurately characterizing the material's structural behavior. The mechanical properties of HC420 steel were calibrated from experimental data as follows: the elastic modulus was 198 MPa, the yield strength was 450 MPa, the ultimate tensile strength was 783 MPa, the elongation was 22%, and the anisotropy coefficient is shown in Figure 3b as the r-value of the material along three loading directions. The chemical composition of the HC420 steel is shown in Table 1.

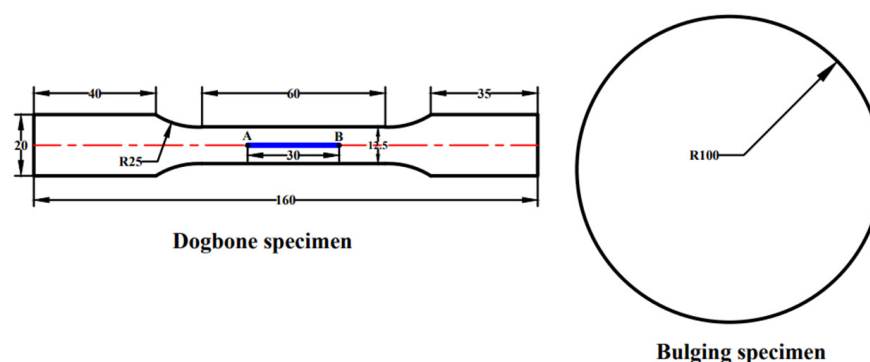


Figure 1. Anisotropic hardening experiment design for HC420 [unit: mm].

Table 1. Chemical compositions of HC420 steel %.

C	Si	Mn	P	S	Al	Nb	Ti
0.10	0.50	1.60	0.025	0.024	0.015	≤0.09	0.15

Uniaxial tensile tests were performed using the universal testing machine at room temperature under quasi-static conditions, as shown in Figure 2. An XTOP three-dimensional digital image correlation (3D-DIC) system with a resolution of 2448×600 pixels was used to record between 200 and 250 images for each experiment during the experiment to measure and analyze the deformation of the specimen. A EF11-100 LED was used throughout the experimental process to enhance DIC calculations by improving contrast and reducing glare on the specimens. Before starting the experiment, spray paint was used to apply uniform black and white speckles on the surface of all specimens. For the dogbone experiment, the crosshead speed was set to 3.6 mm/min, corresponding to a strain rate of 0.001/s under quasi-static conditions. The axial extensometer gauge length was 30 mm, and the stroke was calculated by measuring changes in axial gauge length throughout the experiment by using the GOM 2018 software. To achieve accurate measurement results, the extensometer was positioned in a region where deformation was uniform at both ends of the specimen's parallel zone.

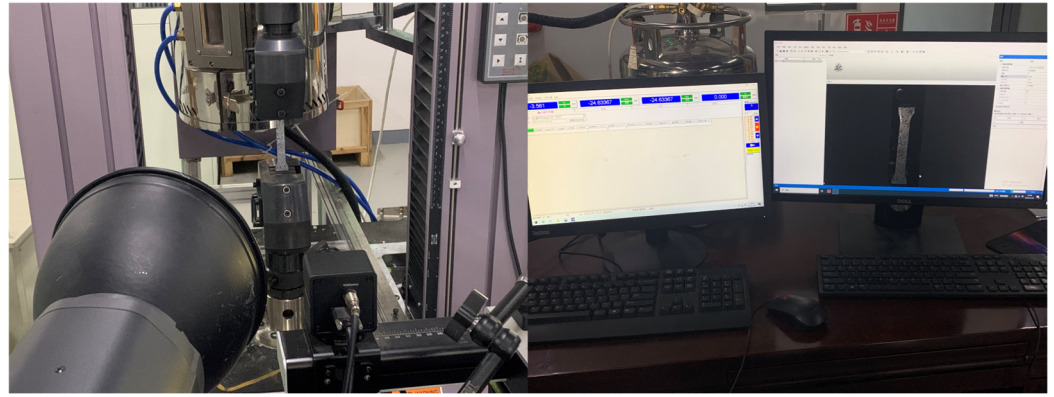


Figure 2. Universal testing machine for tensile tests.

A hydraulic bulging test machine (Zwick, Dortmund, Germany) with a blank holding force of 600 kN was employed to collect test data for HC420 under equibiaxial tension (EBT) circumstances. At least three tests were conducted for each loading direction to guarantee adequate repeatability and reliability of the experiments.

Once the uniaxial tensile tests were finished, the load–stroke curve depicted in Figure 3a was created using the most representative tensile test data along three loading directions: RD, DD, and TD. The ratio of the width strain to the thickness strain of the material is represented by the Lankford coefficient (*r*-value), which represents the ability of the material to exhibit plastic properties under tensile loading. Figure 3b shows the relationship curves between the width strain and the axial strain of dogbone specimens in the RD, DD, and TD directions. Figure 3c shows the evolution of the instantaneous *r*-value, indicating that the plastic potential shape of HC420 changes dramatically during plastic deformation. When the *r*-value is less than 1.0, the material preferentially deforms in the thickness direction rather than in the plane, leading to reduced resistance to thinning and potentially affecting formability. The *r*-value for the EBT is 1.0 and defined as $d\epsilon_y/d\epsilon_x$ by Barlat et al. [6]. Considering that the elastic strain is very small compared with the plastic deformation, the coefficient of equibiaxial anisotropy can also be approximated by the ratio of the $d\epsilon_y/d\epsilon_x$. While the studies are highly repeatable, the material's hardening behavior varies greatly depending on the loading circumstances, according to a comparison of the experimental data processing findings between groups.

The true stress–strain curves for the uniaxial tensile test were computed along the three loading directions of RD, DD, and TD after the load–stroke curves of each group with the best repeatability were chosen. The stress–strain curves for EBT are displayed in Figure 4. Figure 5 compares the stress–strain curves from the tensile and bulging tests with the hardening curves calibrated using the Swift–Voce function as follows:

$$\bar{\sigma} = \alpha K(e_0 + \epsilon^{-p})^n + (1 - \alpha)(A - (A - B)\exp(-C\epsilon^{-p})) \quad (1)$$

where *k* is the strengthening coefficient that accounts for strain rate sensitivity influencing how the material's stress responds to changes in the deformation rate, *n* is the hardening exponent, determining how rapidly the strength of materials increases in response to strain, *e*₀ represents the initial plastic strain, and ϵ^{-p} denotes the equivalent plastic strain. *A*, *B*, and *C* represents the materials yield stress, saturation stress, and hardening rate, respectively. Together, these parameters allow for an accurate description of the flow stress under different loading conditions and capture the hardening response for HC420 steel.

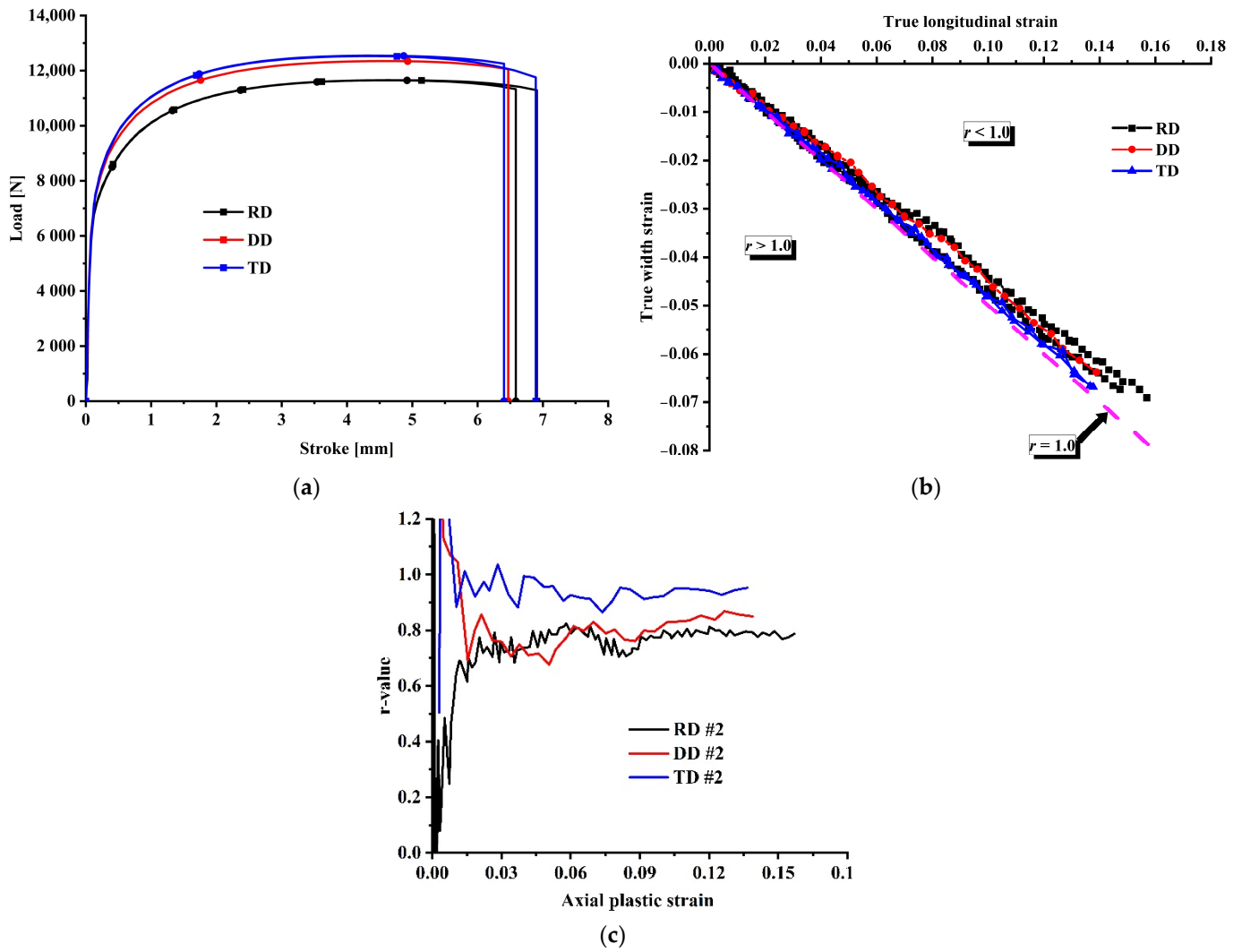


Figure 3. Experimental results of the dogbone specimens in various directions: (a) load–stroke curve; (b) axial strain and width strain for r-value computation; (c) r-value evolution along RD, DD, and TD.

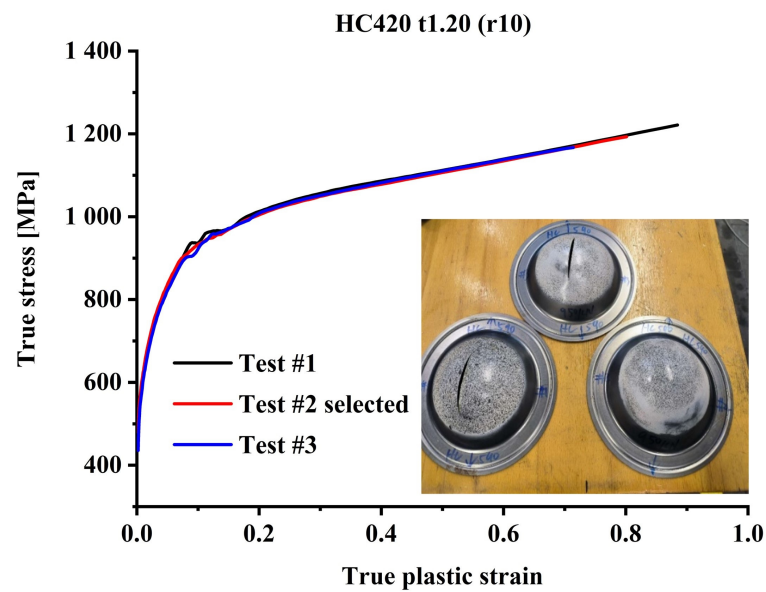


Figure 4. EBT stress–strain curves from bulging tests (blank holding force 600 kN).

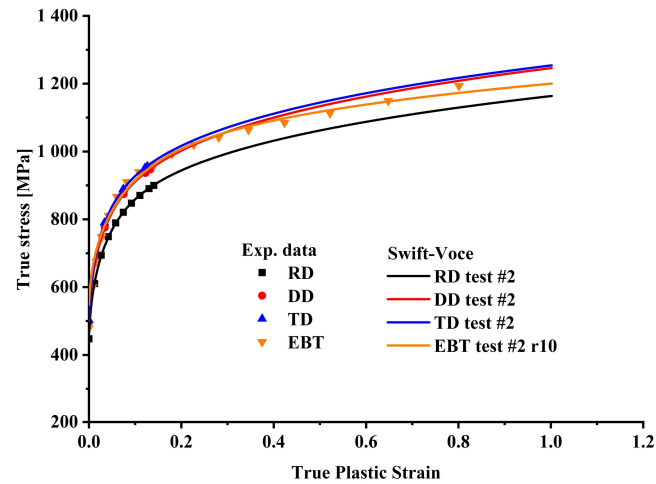


Figure 5. Swift–Voce hardening law and experimental stress–strain curves for the uniaxial and EBT test.

The calibrated curves that fit the test data were satisfying, demonstrating the high accuracy of the Swift–Voce hardening function in describing the hardening behavior of HC420. The results from the Swift–Voce function are shown in Table 2. The hardness curves of the two tests were normalized along RD to enhance their similarity, as shown in Figure 6. It is evident that the hardening curves of the material exhibited notable variations with the change in the loading direction, suggesting that the loading direction can significantly affect the material’s hardening behavior and further proving that HC420 has strong anisotropic hardening characteristics.

Table 2. Mechanical properties of HC420 from the Swift–Voce equation.

Stress State	r-Value	K [MPa]	e_0	n	A [MPa]	B [MPa]	C	α
RD #2	0.8012	1256.24	0.0020	0.1671	897.55	495.35	24.03	0.7403
DD #2	0.8437	1310.93	0.0022	0.1595	943.96	536.38	25.40	0.8217
TD #2	0.9316	1326.76	0.0019	0.1565	951.06	542.42	27.55	0.8046
EBT	1.00	1231.30	0.0020	0.1323	1096.30	572.59	11.51	0.7665

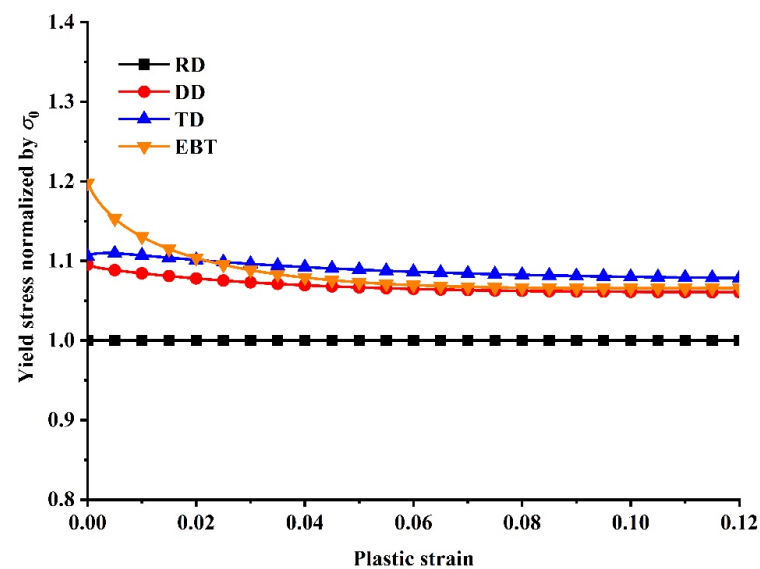


Figure 6. The alloy exhibits an anisotropic hardening tendency.

3. Anisotropic Hardening Functions

Yld2000-2d, Stoughton-Yoon'2009 (S-Y 2009), and the recently suggested Chen-CQN yield functions were chosen for comparison to identify appropriate yield functions for the numerical modeling of HC420.

3.1. Yld2000-2d Function

The Yld2000-2d function for the planar strain issue may be expressed as follows:

$$\varnothing = \varnothing' + \varnothing'' = 2\bar{\sigma}^m \quad (2)$$

where m is the material coefficient and \varnothing' and \varnothing'' are isotropic functions defined as:

$$\varnothing'' = |2X_2'' + X_1''|^m + |2X_1'' + X_2''|^m, \quad \varnothing' = |X_1' - X_2'|^m \quad (3)$$

For BCC metals, the exponent m value should be six, whereas, for FCC metals, it should be eight. Moreover, X_i' and X_j'' are the principal values of the matrices X' and X'' . The following formula was used to determine the two values X_i' and X_j'' :

$$X_i' = \frac{1}{2} \left(X_{11}' + X_{22}' \pm \sqrt{(X_{11}' - X_{22}')^2 + 4X_{12}'^2} \right), \quad X_j'' = \frac{1}{2} \left(X_{11}'' + X_{22}'' \pm \sqrt{(X_{11}'' - X_{22}'')^2 + 4X_{12}''^2} \right) \quad (4)$$

where components of X' and X'' are obtained through the transformation matrix of the Cauchy stress: $X' = L'\sigma$ and $X'' = L''\sigma$. The following are the expressions for the coefficients of L' and L'' :

$$\begin{bmatrix} L_{11}' \\ L_{12}' \\ L_{21}' \\ L_{22}' \\ L_{66}' \end{bmatrix} = \begin{bmatrix} 2/3 & 0 & 0 \\ -1/3 & 0 & 0 \\ 0 & -1/3 & 0 \\ 0 & 2/3 & 0 \\ 0 & 0 & 1 \end{bmatrix} \begin{bmatrix} \alpha_1 \\ \alpha_2 \\ \alpha_7 \end{bmatrix}, \quad \begin{bmatrix} L_{11}'' \\ L_{12}'' \\ L_{21}'' \\ L_{22}'' \\ L_{66}'' \end{bmatrix} = \frac{1}{9} \begin{bmatrix} -2 & 2 & 8 & -2 & 0 \\ 1 & -4 & -4 & 4 & 0 \\ 4 & -4 & -4 & 1 & 0 \\ -2 & 8 & 2 & -2 & 0 \\ 0 & 0 & 1 & 0 & 9 \end{bmatrix} \begin{bmatrix} \alpha_3 \\ \alpha_4 \\ \alpha_5 \\ \alpha_6 \\ \alpha_8 \end{bmatrix} \quad (5)$$

where $\alpha_1 \sim \alpha_8$ are eight anisotropic coefficients that are typically calibrated under EBT using stress and r-values. The following is the calibration minimization function:

$$err = \sum_{i=1}^l w_i \left(\frac{\sigma_i^{exp}}{\sigma_i^{pred}} - 1 \right)^2 + \sum_{j=1}^n w_j \left(\frac{r_j^{exp}}{r_j^{pred}} - 1 \right)^2 \quad (6)$$

where σ_i^{exp} and σ_i^{pred} are the experimental and predicted stress, respectively, and r_j^{exp} and r_j^{pred} are the experimental and predicted r-values, respectively. Parameters W_i and W_j are the weighting factors for stress and the r-value. Both i and j represent data points used to optimize material parameters, typically 0° , 45° , and 90°

3.2. Stoughton-Yoon'2009 Function

The hardening curves generated by various loading directions will vary when the sheet is subjected to proportional loading. This observation challenges the assumption that the yield surface shape remains constant in any isotropic yielding model. It suggests that for anisotropic materials, the yield surface shape is, typically, only consistent during yield hardening. To address this, S-Y 2009 replaces the hardening curves for 0° , 45° , and 90°

and isotropic biaxial tension conditions in the rolling direction under plane stress with the parameters that reflect the initial anisotropy in the Hill48 yield criteria.

$$f_s(\sigma, \bar{\lambda}) = \left(\frac{\sigma_{11}}{\sigma_0^2(\bar{\lambda})} - \frac{\sigma_{22}}{\sigma_{90}^2(\bar{\lambda})} \right) (\sigma_{11} - \sigma_{22}) + \frac{\sigma_{11}\sigma_{22} - \sigma_{12}\sigma_{21}}{\sigma_b^2(\bar{\lambda})} + \frac{4\sigma_{12}\sigma_{21}}{\sigma_{45}^2(\bar{\lambda})} \quad (7)$$

where $\bar{\lambda}$ is the effective plastic strain and $\sigma_0(\bar{\lambda})$, $\sigma_{45}(\bar{\lambda})$, $\sigma_{90}(\bar{\lambda})$, and $\sigma_b(\bar{\lambda})$ align with the hardening results under uniaxial tension conditions along RD, DD, and TD and equibiaxial stress.

3.3. Newly Proposed Coupled Quadratic–Nonquadratic Function

The Chen-CQN model performs well in characterizing the curvature of the yield surface of metals under planar tension circumstances, and the S-Y 2009 yield criteria accurately depict anisotropic hardening under uncorrelated flow rules. To calibrate the yielding behavior and characterize the anisotropic hardening of BCC and FCC under proportional loading circumstances, Chen et al. [38] integrated the strengths of the two yield functions and added the c parameter to the Cazacu'2018 function for BCC and FCC materials.

The yielding function proposed by Cazacu in 2018 looks like the following form:

$$\bar{\sigma}_f(\sigma_{ij}) = a \left(J_2^4 - c J_2 J_3^2 \right)^{1/8} \quad (8)$$

where the parameter a can be expressed as:

$$a = \left(\frac{81 \times 27}{27 - 4c} \right)^{\frac{1}{8}} \quad (9)$$

The yielding behavior of the BCC and FCC materials is calibrated by the values of 1.5776 and 2.5116 for the parameter c in the Cazacu'2018 yield function, respectively. The value of c has a significant impact on the development of the yield surface. The J_2 and J_3 are the second and third invariants of the stress deviator, respectively. The formulas of the invariants J_2 and J_3 are defined as follows:

$$J_2 = -s_1s_2 - s_2s_3 - s_1s_3 \quad (10)$$

$$J_3 = s_1s_2s_3 \quad (11)$$

where s_1 , s_2 , and s_3 are principal invariants of the deviatoric stress tensor s . The Cazacu'2018 yield function may be extended to anisotropic hardening based on the CQN model by substituting the modified Hill48 yield function in the S-Y 2009 function for the Cazacu'2018 yield function's pressure invariant J_2 .

$$\bar{\sigma}_f(\sigma_{ij}) = b \left[J_2 \left(J_2^3 - c J_3^2 \right) \right]^{1/8} \quad (12)$$

$$f_c(\sigma, \bar{\lambda}) = [f_{Hill48}(\sigma, \bar{\lambda}) \cdot f_{Drucker}(\sigma)]^{\frac{1}{8}} = 1 \quad (13)$$

with

$$\begin{aligned} f_{Hill48}(\sigma, \bar{\lambda}) &= F(\bar{\lambda})(\sigma_{22} - \sigma_{33})^2 + G(\bar{\lambda})(\sigma_{33} - \sigma_{11})^2 + H(\bar{\lambda})(\sigma_{11} - \sigma_{22})^2 \\ &\quad + 2L(\bar{\lambda})\sigma_{23}^2 + 2M(\bar{\lambda})\sigma_{31}^2 + 2N(\bar{\lambda})\sigma_{12}^2 \\ f_{Drucker}(\sigma) &= a(J_2^3 - cJ_3^2) \end{aligned} \quad (14)$$

where $f_{\text{Drucker}}(\sigma)$ is the Drucker function, $f_{\text{Hill48}}(\sigma, \bar{\lambda})$ is an anisotropic hardening function based on Hill48, and Equation (12) is a rearrangement of the Cazacu'2018 yield function.

The six parameters of the Hill48 are functions of the hardening along three directions, and these parameters are defined as follows:

$$\begin{aligned}
 F(\bar{\lambda}) &= \frac{1}{2} \left(\frac{1}{[\sigma_{90}(\bar{\lambda})]^8} + \frac{1}{[\sigma_{ND}(\bar{\lambda})]^8} - \frac{1}{[\sigma_0(\bar{\lambda})]^8} \right) \\
 G(\bar{\lambda}) &= \frac{1}{2} \left(\frac{1}{[\sigma_0(\bar{\lambda})]^8} + \frac{1}{[\sigma_{ND}(\bar{\lambda})]^8} - \frac{1}{[\sigma_{90}(\bar{\lambda})]^8} \right) \\
 H(\bar{\lambda}) &= \frac{1}{2} \left(\frac{1}{[\sigma_0(\bar{\lambda})]^8} + \frac{1}{[\sigma_{90}(\bar{\lambda})]^8} - \frac{1}{[\sigma_{ND}(\bar{\lambda})]^8} \right) \\
 L(\bar{\lambda}) &= \frac{1}{2[\tau_{yz}(\bar{\lambda})]^8} \\
 M(\bar{\lambda}) &= \frac{1}{2[\tau_{xz}(\bar{\lambda})]^8} \\
 N(\bar{\lambda}) &= \frac{1}{2[\tau_{xy}(\bar{\lambda})]^8}
 \end{aligned} \tag{15}$$

where $\tau_{yz}(\bar{\lambda})$, $\tau_{xz}(\bar{\lambda})$, and $\tau_{xy}(\bar{\lambda})$ are the shear hardening curves in the yz , xz , and xy planes, while $\sigma_0(\bar{\lambda})$, $\sigma_{90}(\bar{\lambda})$, and $\sigma_{ND}(\bar{\lambda})$ are the hardening curves for uniaxial stretching conditions along the rolling direction (RD), transverse direction (TD), and normal direction (ND). Equation (15) is expressed under a full three-dimensional stress state, while the Yld2000-2d and S-Y 2009 yield functions are formulated for plane stress conditions, neglecting any out-of-plane stresses. This indicates the important role of the invariants J_2 and J_3 in Equations (10) and (11) in characterizing the yield behavior of materials under complex loading conditions.

4. Convexity Analysis

It is evident from the earlier analysis of Figure 6 that HC420 exhibits clear anisotropic properties in uniaxial tension under various loading scenarios, and that the hardening behavior of HC420 varies under the two stress states of uniaxial and EBT. Additionally, the likelihood of the material displaying surface convexity decreases due to the variation in plastic strain across stress levels. Thus, further research on the yield function's convexity is required in this work.

In the Chen-CQN yield model, the associated plastic strain $\bar{\lambda}$ significantly influences the anisotropic properties of the material, whereas parameter c governs the curvature of the yield locus. Thus, both c and $\bar{\lambda}$ define the convexity of the yield surface in the model. In this study, the newly proposed geometry-inspired numerical convex analysis (GINCA) approach is used to examine the convexity of the yield surface. The GINCA approach has been developed to evaluate the convexity of yield functions. The GINCA approach focuses on the effective stress derived from the yield function, eliminating the need to calculate first- and second-order partial derivatives. The effectiveness of the GINCA method has been verified by applying it to various well-established yield functions, including those proposed by Cazacu–Barlat (2004), Cazacu (2018), and Drucker and Hu (2017). In addition, it has been used to determine the convexity of the yield function of Gao (2011), which had not been previously defined. The GINCA approach has also been used to analyze the evolution of convex domains concerning plastic deformation in anisotropic hardening functions and

to investigate the convexity of polynomial yield functions relevant to strongly anisotropic metals [39]. As shown in Figure 7, the convex domain represented by the region between the two red solid lines is mapped by varying the parameters c and $\bar{\lambda}$ under circumstances of plane stress and equibiaxial loading. It is evident that the $\bar{\lambda}$ determines the critical value of c required to ensure the yield function adheres to the condition of external convexity.

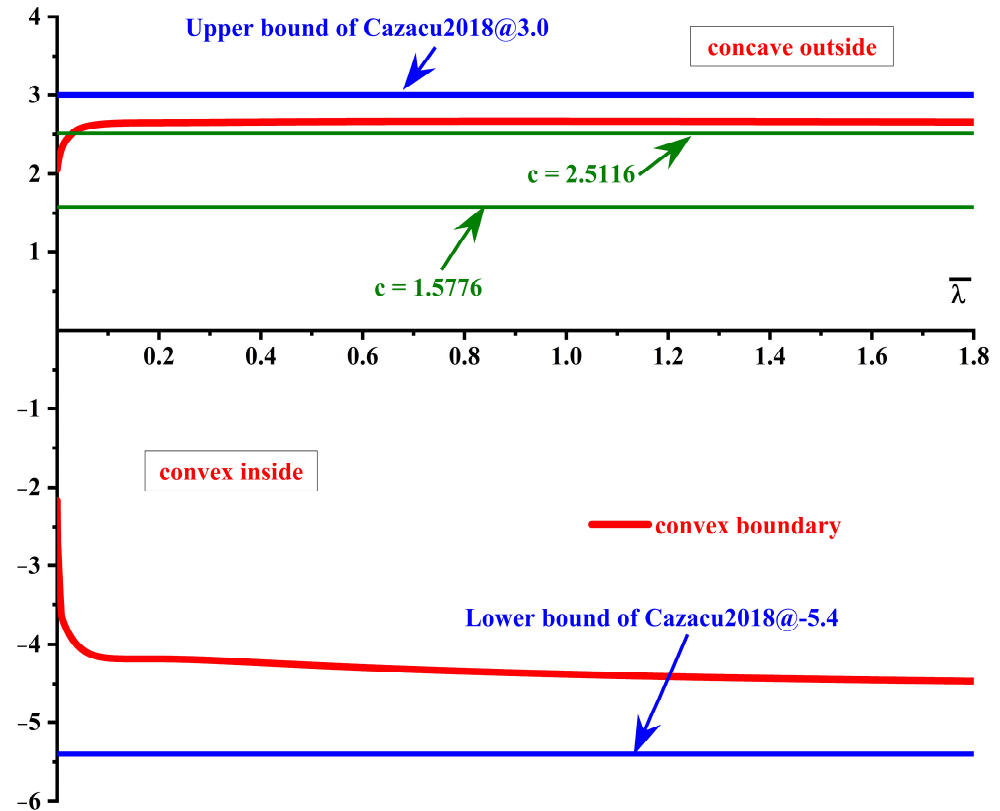


Figure 7. Convex domain of the Chen-CQN model for HC420 calculated by GINCA.

The convex domains of both functions were compared, as the anisotropic Chen-CQN model simplifies into the isotropic Cazacu'2018 model when applied to isotropic materials. The boundary of the convex domain for the Cazacu'2018 model is represented by the solid blue line in Figure 7. It is clear that the convex domain of the Cazacu'2018 function entirely encompasses that of the Chen-CQN function. This phenomenon occurs because increasing material anisotropy in the Chen-CQN model reduces its convex domain, thereby increasing the likelihood of yield surface distortion.

As long as the effective plastic strain $\bar{\lambda}$ is within the range $[0, 1.8]$ in Figure 7, the hardening law for HC420, a BCC material, stays inside the convex domain. The yield surfaces for the two sites $\bar{\lambda} = 0.0067, c = 2.5116$, and $\bar{\lambda} = 1.5, c = 2.5116$ are shown in Figure 8. Red dots indicate areas of the yield surfaces that are depressed. As seen in Figure 8a, the yield surface is concave because the point $\bar{\lambda} = 0.0067$ and $c = 2.5116$ is beyond the convex domain. Here, the plane strain state is surrounded by four concave regions. On the other hand, the convex with no concave areas is at point $\bar{\lambda} = 1.5$ and $c = 2.5116$.

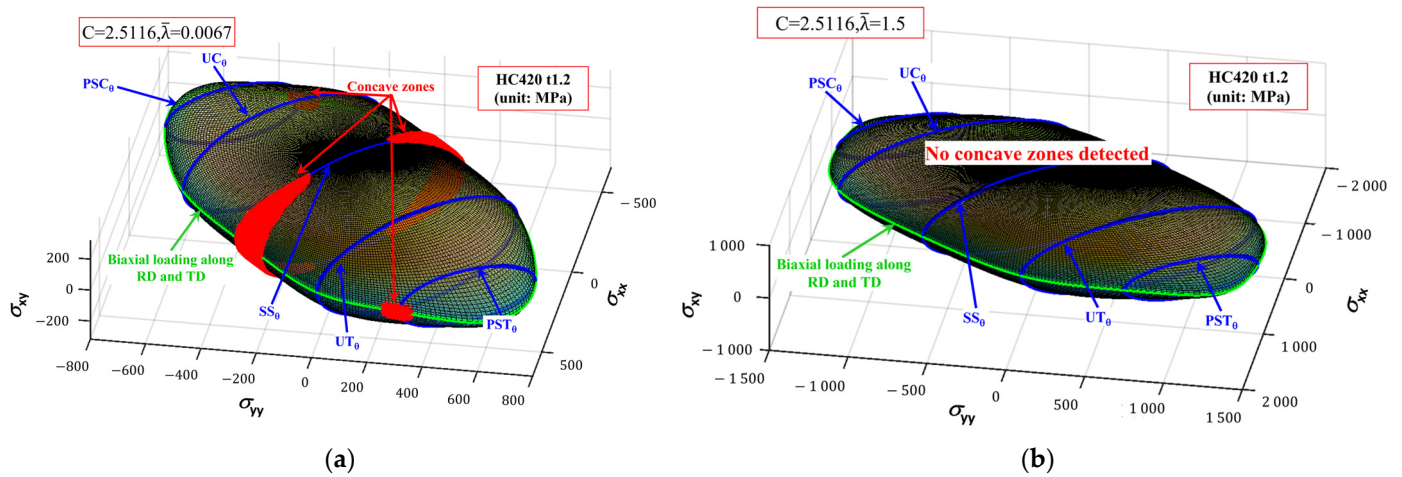


Figure 8. Chen-CQN surface convexity investigation at two specific locations in Figure 7: (a) is concave and (b) is convex.

5. Results

To validate whether the yield function accurately describes the anisotropic features of HC420, the expected yield trajectories obtained from the Yld2000-2d, S-Y 2009, and Chen-CQN yield functions were compared with experimental observations. The calibrated coefficient values of the Yld2000-2d model at different levels of plastic strain in HC420 were derived from the hardening curve data of the material and are summarized in Table 3.

Table 3. Coefficients of the Yld2000-2d function.

λ	α_1	α_2	α_3	α_4	α_5	α_6	α_7	α_8	m
0.002	0.9988	0.8812	0.9780	0.9470	0.9739	0.7950	0.9235	0.9800	6
0.10	1.0034	0.8752	0.9852	0.9464	0.9739	0.7968	0.9243	0.9798	6
0.20	0.9988	0.8812	0.9780	0.9470	0.9739	0.7950	0.9235	0.9800	6

Figure 9 shows the development of the yield surface for HC420 corresponding to various equivalent plastic stresses based on the three yield functions, against the experimental results in biaxial tensile tests. The S-Y 2009 and Chen-CQN yield functions accurately defined the yield surface during initial yielding, while the Yld2000-2d yield function offered a slightly less accurate fit to the experimental data. However, as the associated plastic strain increased, the accuracy of the Yld2000-2d yield function diminished. This decline is attributed to its inherent isotropic hardening characteristics, which become less effective in capturing the behavior of the material-evolving plastic. In turn, the S-Y 2009 and Chen-CQN yield functions retained high accuracy, offering a nearly perfect description of the yield surface of HC420 at high strains.

Figure 10 shows the yield surface predictions of HC420 under geographic loading in the π -plane using the Chen-CQN and S-Y 2009 methods. The solid and dashed lines represent the Chen-CQN and S-Y 2009 yield functions, respectively, while the points represent the experimental results. The Chen-CQN function predicts lower yield stress values under the plane stress conditions than the Yld2000-2d method. Therefore, the Yld2000-2d function was excluded due to its poor predictive effectiveness in evaluating the experimental data, so the Chen-CQN method is more accurate when predicting the yield surface of HC420 steel. Figure 11 compares the yield stress predicted by the Chen-CQN model for the uniaxial tensile loading of HC420 along RD, TD, and DD with experimentally measured yield stresses. With increasing plastic strain, the predicted yield stress values

strongly agreed with the empirical measurements, confirming the remarkably high accuracy of the Chen-CQN model in describing the uniaxial tensile yield stresses of HC420 under different strains.

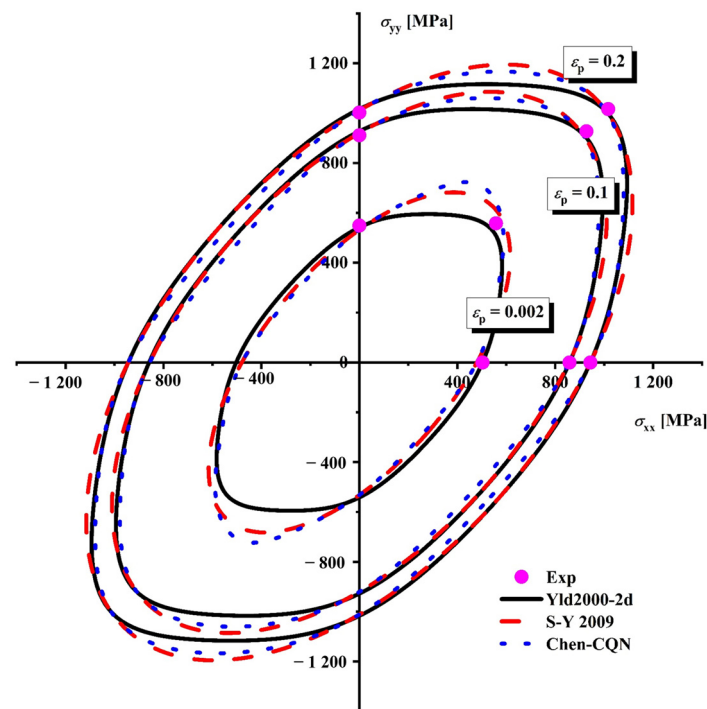


Figure 9. Comparison of the yield surface evolution under biaxial loading along RD, DD, and TD ($c = 2.0$) between the predictions and the experiments.

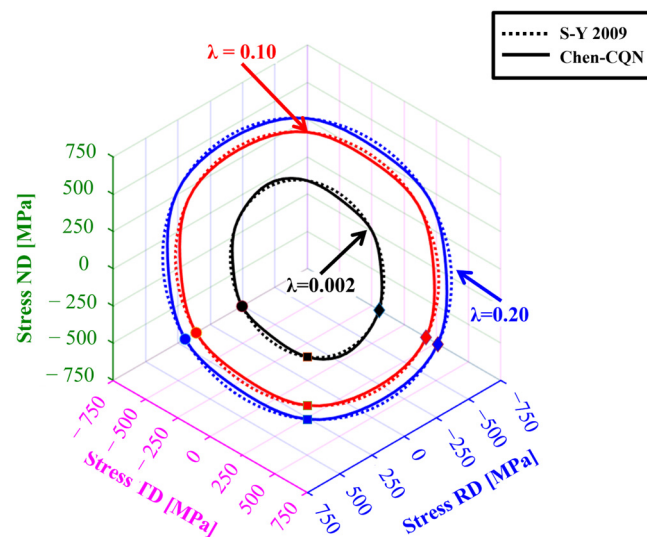


Figure 10. Comparison of the yield surface development on the π -plane between the predictions and the experiments.

Figure 12 compares the hardening curves of HC420 under uniaxial stress at three loading orientations, i.e., RD, DD, and TD, with experimental data and under EBT for predictions by the Chen-CQN yield function. It is seen that the predicted uniaxial tensile anisotropic hardening curves agreed closely with the actual data, with only a small deviation between the predicted and experimental curves under EBT. The prediction error between the Chen-CQN and experimental stress was calculated using Equation (16), and the prediction error is shown in Figure 12b; the largest inaccuracy in the Chen-CQN func-

tion’s predictions of hardening curves during plastic deformation under uniaxial strain was consistently less than 1%. Furthermore, the prediction error gradually diminished as the strain rose, finally nearing zero. Under EBT circumstances, the highest inaccuracy occurred at the start of plastic deformation, when irregularities in the material’s hardening curve were more noticeable, resulting in significantly lower forecast accuracy. However, throughout the plastic deformation process, up to necking, the difference between the prediction and experimental curves under equibiaxial stress was less than 2%. These findings demonstrate that the anisotropic hardening behavior of HC420 is accurately characterized by the Chen-CQN yield function and meets the required accuracy standards for numerical simulations.

$$\%Error = \left(\frac{\sigma_i^{pred}}{\sigma_i^{exp}} - 1 \right) \times 100 \tag{16}$$

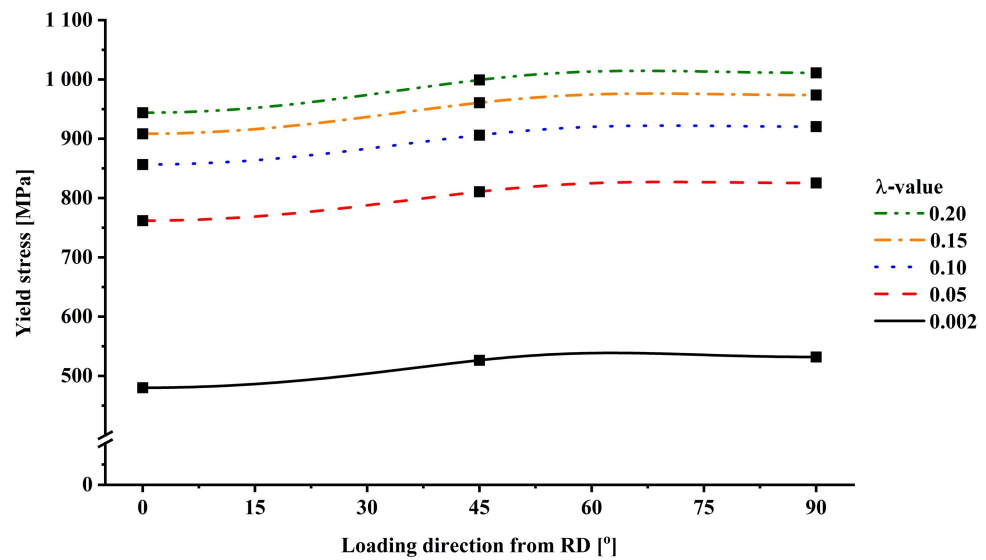


Figure 11. Uniaxial tensile yield stress progression between the forecast and the experiment is compared.

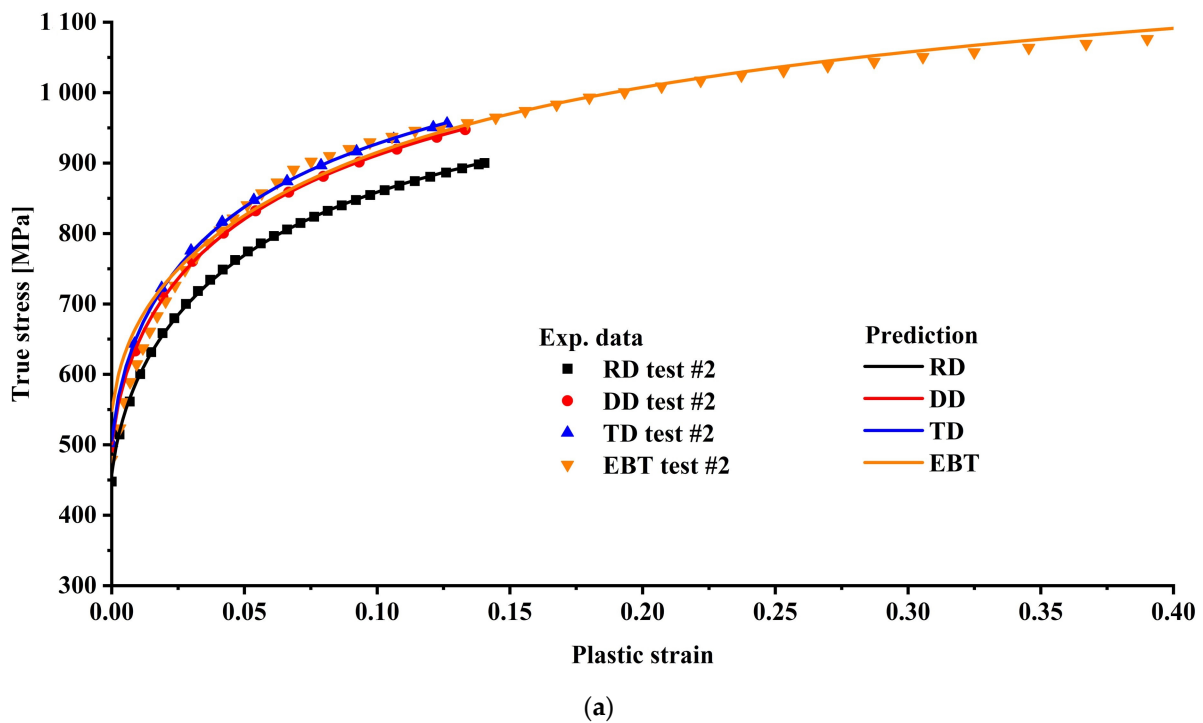


Figure 12. Cont.

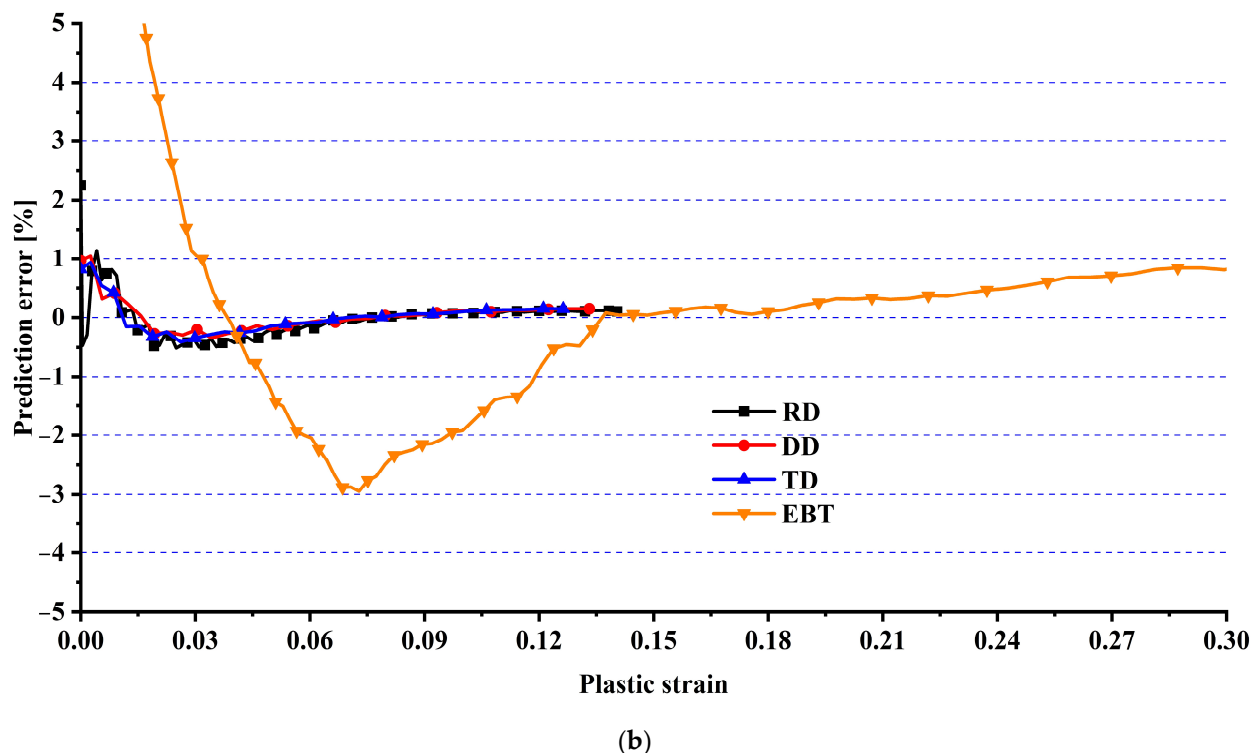


Figure 12. Hardening curves of HC420 under uniaxial and EBT: (a) stress–strain curves for uniaxial and EBT are compared between predictions and experiments and (b) prediction inaccuracy of uniaxial and EBT stress–strain curves.

6. Conclusions

In this study, uniaxial tensile tests in three directions and EBT tests are performed for HC420 steel to obtain hardening data. The Chen-CQN approach is applied to characterize the anisotropic hardening behavior, and the convexity of the yield surface of the Chen-CQN approach is verified using the dichotomous method. The experimental data are combined with Chen-CQN approach predictions, and the hardening behavior predictions of the Chen-CQN approach are compared with the yield functions Yld2000-2d and S-Y 2009. The results of the study are as follows:

1. The results show anisotropic behavior in the plastic deformation of HC420 steel, such a behavior being crucial for its use in lightweight automotive applications.
2. The Chen-CQN function shows high accuracy in predicting the anisotropic hardening behavior of HC420 steel under varying stress conditions, whereas the Chen-CQN function results show a prediction error of less than 2%.
3. The Chen-CQN function shows superiority in yield stress prediction and clearer numerical implementation compared with Yld2000-2d and S-Y 2009 yield functions.
4. The Chen-CQN function shows its ability to combine high accuracy and flexibility in determining the anisotropic behavior of HC420 steel.

Author Contributions: Conceptualization, T.S.A. and Y.L.; methodology, T.S.A. and Y.L.; software, T.S.A. and A.I.C.; validation, T.S.A., H.A. and A.I.C.; formal analysis, T.S.A. and H.A.; investigation, T.S.A. and A.I.C.; resources, Y.L.; data curation, T.S.A.; writing—original draft preparation, T.S.A., H.A. and A.I.C.; writing—review and editing, Y.L.; visualization, T.S.A. and Y.L.; supervision, Y.L.; project administration, Y.L.; funding acquisition, Y.L. All authors have read and agreed to the published version of the manuscript.

Funding: The authors acknowledge the financial support by the National Natural Science Foundation of China (Grant No. 52075423; U2141214).

Data Availability Statement: The raw data supporting the conclusions of this article will be made available by the authors on request.

Conflicts of Interest: The authors declare no conflicts of interest.

References

- Galán, J.; Samek, L.; Verleysen, P.; Verbeken, K.; Houbaert, Y. Advanced High Strength Steels for Automotive Industry. *Rev. Metal.* **2012**, *48*, 118–131. [[CrossRef](#)]
- Lu, C.W.; Hung, F.Y.; Chang, T.W.; Hsieh, H.Y. Study and Application on the Electromagnetic Stainless Steel: Microstructure, Tensile Mechanical Behavior, and Magnetic Properties. *Materials* **2024**, *17*, 2998. [[CrossRef](#)] [[PubMed](#)]
- Hu, Q.; Zhang, F.; Li, X.; Chen, J. Overview on the Prediction Models for Sheet Metal Forming Failure: Necking and Ductile Fracture. *Acta Mech. Solida Sin.* **2018**, *31*, 259–289. [[CrossRef](#)]
- Hou, Y.; Min, J.; Stoughton, T.B.; Lin, J.; Carsley, J.E.; Carlson, B.E. A Non-Quadratic Pressure-Sensitive Constitutive Model under Non-Associated Flow Rule with Anisotropic Hardening: Modeling and Validation. *Int. J. Plast.* **2020**, *135*, 102808. [[CrossRef](#)]
- You, J.; Liu, J.; Zhou, C.; Gao, W.; Yao, Y. Anisotropic Hardening and Plastic Evolution Characterization on the Pressure-Coupled Drucker Yield Function of ZK61M Magnesium Alloy. *Materials* **2024**, *17*, 1150. [[CrossRef](#)] [[PubMed](#)]
- Barlat, F.; Brem, J.C.; Yoon, J.W.; Chung, K.; Dick, R.E.; Lege, D.J.; Pourboghrat, F.; Choi, S.-H.; Chu, E. Plane Stress Yield Function for Aluminum Alloy Sheets—Part 1: Theory. *Int. J. Plast.* **2003**, *19*, 1297–1319. [[CrossRef](#)]
- Banabic, D.; Aretz, H.; Comsa, D.S.; Paraianu, L. An Improved Analytical Description of Orthotropy in Metallic Sheets. *Int. J. Plast.* **2005**, *21*, 493–512. [[CrossRef](#)]
- Aretz, H.; Barlat, F. New Convex Yield Functions for Orthotropic Metal Plasticity. *Int. J. Non. Linear Mech.* **2013**, *51*, 97–111. [[CrossRef](#)]
- Mu, Z.; Wang, W.; Zhang, S.; Zheng, Z.; Yan, H.; Liu, S.; Ma, S.; Du, K.; Hou, Y. Towards Improved Description of Plastic Anisotropy in Sheet Metals under Biaxial Loading: A Novel Generalization of Hill48 Yield Criterion. *Mater. Today Commun.* **2024**, *41*, 110222. [[CrossRef](#)]
- Kim, J.H.; So, J.H.; Koo, H.J. Facile Formation of Metallic Surface with Microroughness via Spray-Coating of Copper Nanoparticles for Enhanced Liquid Metal Wetting. *Materials* **2024**, *17*, 5299. [[CrossRef](#)]
- Lou, Y.; Zhang, C.; Wu, P.; Whan Yoon, J. New Geometry-Inspired Numerical Convex Analysis Method for Yield Functions under Isotropic and Anisotropic Hardenings. *Int. J. Solids Struct.* **2024**, *286*, 286–287. [[CrossRef](#)]
- Barlat, F.; Aretz, H.; Yoon, J.W.; Karabin, M.E.; Brem, J.C.; Dick, R.E. Linear Transformation-Based Anisotropic Yield Functions. *Int. J. Plast.* **2005**, *21*, 1009–1039. [[CrossRef](#)]
- Cazacu, O. New Yield Criteria for Isotropic and Textured Metallic Materials. *Int. J. Solids Struct.* **2018**, *139–140*, 200–210. [[CrossRef](#)]
- Cazacu, O. New Mathematical Results and Explicit Expressions in Terms of the Stress Components of Barlat et Al. (1991) Orthotropic Yield Criterion. *Int. J. Solids Struct.* **2019**, *176–177*, 86–95. [[CrossRef](#)]
- Park, N.; Stoughton, T.B.; Yoon, J.W. A Criterion for General Description of Anisotropic Hardening Considering Strength Differential Effect with Non-Associated Flow Rule. *Int. J. Plast.* **2019**, *121*, 76–100. [[CrossRef](#)]
- Lou, Y.; Zhang, C.; Zhang, S.; Yoon, J.W. A General Yield Function with Differential and Anisotropic Hardening for Strength Modelling under Various Stress States with Non-Associated Flow Rule. *Int. J. Plast.* **2022**, *158*, 103414. [[CrossRef](#)]
- Drucker, D.C. Relation of Experiments to Mathematical Theories of Plasticity. *J. Appl. Mech. Trans. ASME* **1949**, *16*, 349–357. [[CrossRef](#)]
- Barlat, F.; Maeda, Y.; Chung, K.; Yanagawa, M.; Brem, J.C.; Hayashida, Y.; Lege, D.J.; Matsui, K.; Murtha, S.J.; Hattori, S.; et al. Yield Function Development for Aluminum Alloy Sheets. *J. Mech. Phys. Solids* **1997**, *45*, 1727–1763. [[CrossRef](#)]
- Hu, Q.; Yoon, J.W. Anisotropic Distortional Hardening Based on Deviatoric Stress Invariants under Non-Associated Flow Rule. *Int. J. Plast.* **2022**, *151*, 103214. [[CrossRef](#)]
- Lee, E.H.; Mallett, R.L.; Wertheimer, T.B. Stress Analysis for Anisotropic Hardening in Finite-Deformation Plasticity. *Am. Soc. Mech. Eng.* **1983**, *50*, 554–560. [[CrossRef](#)]
- Hu, Q.; Yoon, J.W.; Manopulo, N.; Hora, P. A Coupled Yield Criterion for Anisotropic Hardening with Analytical Description under Associated Flow Rule: Modeling and Validation. *Int. J. Plast.* **2021**, *136*, 102882. [[CrossRef](#)]
- Hou, Y.; Min, J.; Lin, J.; Lee, M.G. Modeling Stress Anisotropy, Strength Differential, and Anisotropic Hardening by Coupling Quadratic and Stress-Invariant-Based Yield Functions under Non-Associated Flow Rule. *Mech. Mater.* **2022**, *174*, 104458. [[CrossRef](#)]
- Lou, Y.; Yoon, J.W. Lode-Dependent Anisotropic-Asymmetric Yield Function for Isotropic and Anisotropic Hardening of Pressure-Insensitive Materials. Part I: Quadratic Function under Non-Associated Flow Rule. *Int. J. Plast.* **2023**, *166*, 103647. [[CrossRef](#)]

24. Stoughton, T.B.; Yoon, J.W. Anisotropic Hardening and Non-Associated Flow in Proportional Loading of Sheet Metals. *Int. J. Plast.* **2009**, *25*, 1777–1817. [[CrossRef](#)]
25. Du, K.; Huang, S.; Li, X.; Wang, H.; Zheng, W.; Yuan, X. Evolution of Yield Behavior for AA6016-T4 and DP490—Towards a Systematic Evaluation Strategy for Material Models. *Int. J. Plast.* **2022**, *154*, 103302. [[CrossRef](#)]
26. Hou, Y.; Du, K.; El-Aty, A.A.; Lee, M.G.; Min, J. Plastic Anisotropy of Sheet Metals under Plane Strain Loading: A Novel Non-Associated Constitutive Model Based on Fourth-Order Polynomial Functions. *Mater. Des.* **2022**, *223*, 111187. [[CrossRef](#)]
27. Lee, E.H.; Choi, H.; Stoughton, T.B.; Yoon, J.W. Combined Anisotropic and Distortion Hardening to Describe Directional Response with Bauschinger Effect. *Int. J. Plast.* **2019**, *122*, 73–88. [[CrossRef](#)]
28. Barlat, F.; Yoon, J.W.; Cazacu, O. On Linear Transformations of Stress Tensors for the Description of Plastic Anisotropy. *Int. J. Plast.* **2007**, *23*, 876–896. [[CrossRef](#)]
29. Barlat, F.; Lian, J. Plastic Behavior and Stretchability of Sheet Metals. Part I: A Yield Function for Orthotropic Sheets under Plane Stress Conditions. *Int. J. Plast.* **1989**, *5*, 51–66. [[CrossRef](#)]
30. Hou, Y.; Lee, M.G.; Lin, J.; Min, J. Experimental Characterization and Modeling of Complex Anisotropic Hardening in Quenching and Partitioning (Q&P) Steel Subject to Biaxial Non-Proportional Loadings. *Int. J. Plast.* **2022**, *156*, 103347. [[CrossRef](#)]
31. Du, K.; Huang, S.; Wang, H.; Yu, F.; Pan, L.; Huang, H.; Zheng, W.; Yuan, X. Effect of Different Yield Criteria and Material Parameter Identification Methods on the Description Accuracy of the Anisotropic Behavior of 5182-O Aluminum Alloy. *J. Mater. Eng. Perform.* **2022**, *31*, 1077–1095. [[CrossRef](#)]
32. Hou, Y.; Min, J.; Guo, N.; Shen, Y.; Lin, J. Evolving Asymmetric Yield Surfaces of Quenching and Partitioning Steels: Characterization and Modeling. *J. Mater. Process. Technol.* **2021**, *290*, 116979. [[CrossRef](#)]
33. Hou, Y.; Myung, D.; Park, J.K.; Min, J.; Lee, H.R.; El-Aty, A.A.; Lee, M.G. A Review of Characterization and Modelling Approaches for Sheet Metal Forming of Lightweight Metallic Materials. *Materials* **2023**, *16*, 836. [[CrossRef](#)] [[PubMed](#)]
34. Lou, Y.; Zhang, S.; Yoon, J.W. Strength Modeling of Sheet Metals from Shear to Plane Strain Tension. *Int. J. Plast.* **2020**, *134*, 102813. [[CrossRef](#)]
35. Park, N.; Stoughton, T.B.; Yoon, J.W. A New Approach for Fracture Prediction Considering General Anisotropy of Metal Sheets. *Int. J. Plast.* **2020**, *124*, 199–225. [[CrossRef](#)]
36. Kuwabara, T.; Mori, T.; Asano, M.; Hakoyama, T.; Barlat, F. Material Modeling of 6016-O and 6016-T4 Aluminum Alloy Sheets and Application to Hole Expansion Forming Simulation. *Int. J. Plast.* **2017**, *93*, 164–186. [[CrossRef](#)]
37. Du, K.; Cui, J.; Hou, Y.; Ren, Y.; You, J.; Ying, L.; Li, X.; Zuo, X.; Huang, H.; Yuan, X. Breaking through the Plasticity Modeling Limit in Plane Strain and Shear Loadings of Sheet Metals by a Novel Additive-Coupled Analytical Yield Criterion. *J. Mater. Sci. Technol.* **2024**, *225*, 261–276. [[CrossRef](#)]
38. Chen, Z.; Wang, Y.; Lou, Y. User-Friendly Anisotropic Hardening Function with Non-Associated Flow Rule under the Proportional Loadings for BCC and FCC Metals. *Mech. Mater.* **2022**, *165*, 104190. [[CrossRef](#)]
39. Wang, J.; Pi, A.; Zhang, Z.; Wu, M.; Huang, F.; Wang, Z.; Hao, F. A Symmetric and Asymmetric Yield Function Based on Normalized Stress Invariant Suitable for Sheet and Bulk Metals under Various Stress States. *J. Mater. Process. Technol.* **2025**, *337*, 118728. [[CrossRef](#)]

Disclaimer/Publisher’s Note: The statements, opinions and data contained in all publications are solely those of the individual author(s) and contributor(s) and not of MDPI and/or the editor(s). MDPI and/or the editor(s) disclaim responsibility for any injury to people or property resulting from any ideas, methods, instructions or products referred to in the content.